Integrated Computer-Aided Engineering 19 (2012) 3–22
DOI 10.3233/ICA-2012-0390
IOS Press

Improved ultra wideband-based tracking of twin-receiver automated guided vehicles

Stefano Busanelli* and Gianluigi Ferrari
Wireless Ad-hoc and Sensor Networks (WASN) Lab, Department of Information Engineering, University of Parma, Parma, Italy

Abstract. In this paper, we present the design and performance analysis of an innovative system for tracking Automated Guided Vehicles (AGVs) in indoor industrial scenarios. An on-board odometer provides information about the dynamic state of the AGV, allowing to predict its pose (i.e., its position and orientation). At the same time, an external Ultra-Wide Band (UWB) wireless network provides the information necessary to compensate for the error drift accumulated by the odometer. Two novel alternative solutions for AGV tracking are proposed: (i) a classical Time Differences Of Arrivals (TDOA) approach with a single receiver; (ii) a "Twin-receiver" TDOA (TTDOA) approach, that requires the presence of two independent receivers on the AGV. The TTDOA configuration allows to indirectly estimate the orientation of the vehicle, thus increasing the estimation accuracy. Moreover, this allows direct estimation of the vehicle's movement even when the odometer is not working properly (e.g., temporary failure) or when the AGV is not moving (e.g., at the start-up). The system performance with the two proposed tracking algorithms is evaluated in realistic conditions, by considering a consolidated UWB channel model and a simple on-board energy detector receiver. The impact of the wireless network architecture and of the presence of moving obstacles is analyzed. The obtained results show clearly that the implementation of a tracking system with a sub-centimeter accuracy can be realized by means of low-complexity UWB receiver and commercial odometers. The automatic movement of goods within a warehouse is one of the most appealing application of the proposed tracking system.

Keywords: Ultra wideband, UWB, automated guided vehicle, AGV, localization, tracking, time difference of arrivals, TDOA

1. Introduction

Following the pioneering work of Win and Scholtz [35], in recent years Ultra-Wide Band (UWB) radio technology has appeared as a technology able to offer a high level of precision with limited costs [14]. According to the Federal Communications Commission (FCC) definition, a UWB signal has an absolute bandwidth of at least 500 MHz or a fractional bandwidth larger than 20% [1]. It is well-known that the precision of the Time-Of-Arrival (TOA) method, for estimating the distance between two devices, is directly proportional to the signal bandwidth. Thanks to its large bandwidth, the use of UWB technology allows to achieve a centimeter-grade (or even higher) precision [13]. According to many experimental campaigns [23], this limit is reachable. In fact, currently available commercial systems are not far from these limits, since they claim a precision on the order of $10 \div 15$ cm, despite the challenging indoor multi-path communication channel that characterizes most industrial buildings [33]. Nowadays, besides the large number of proprietary solutions, only two international UWB standards have been specified: (i) the ECMA 368 [11], based on an Orthogonal Frequency Division Modulation (OFDM)-UWB technology; (ii) the IEEE 802.15.4a [19], an extension of the IEEE 802.15.4 standard, based on the Impulse Radio (IR) technology. In the near future, thanks to the continuous improvements of electronics and the various on-going standardization efforts, there is hope that this technology will become more accurate, yet less expensive.

A precision in the order of tens of centimeters is usually sufficient to meet the requirements of several

*Corresponding author. E-mail: stefano.busanelli@unipr.it.

ISSN 1069-2509/12/$27.50 © 2012 – IOS Press and the author(s). All rights reserved

industrial processes. However, there also applications requiring a significantly higher level of precision. One of the most representative example is given by the precision required by Automated Guided Vehicles (AGVs) used for automatic displacement of goods and assets in factories, which is becoming a common practice in several industrial segments (e.g., food, beverages, paper-tissues). In this type of application, the AGVs move heavy goods (tons) inside a building or between a building and trucks. In this context, a centimeter-grade precision and the repeatability of the measurements are required to prevent damages to infrastructures and workers. For AGV navigation applications with strict real-time requirements, the most common solution consists in fusing together the information obtained by two different systems: (i) an on-board vehicle system, such as an odometer, that offers estimation in the local robot frame (local localization); and (ii) an external positioning system, that provides position estimation in an absolute coordinates system (absolute localization). For example, in [20] the authors combine the information provided by an absolute localization system, given by the Global Positioning System (GPS), with the relative estimation offered by the plethora of sensors that normally equip vehicles. Fusion of local and absolute position estimates can be carried out by Extended Kalman Filtering (EKF) [32] (or derived filters) or by sequential filtering techniques, such as particle filtering [28]. However, the iterative nature of the latter type of filtering will unlikely match the strict real-time requirements of an AGV guidance system.

Depending on the application domain, one can find different solutions for the absolute localization problem. The simpler systems are based on the creation of artificial tracks, by means of buried guide wires or optical beacons, that the AGV has to follow. More refined solutions allow the AGV to move relatively freely in indoor environments. In particular, laser-based systems are probably the most widely adopted, thanks to their high precision and reliability [32]. A non exhaustive list of possible alternatives includes vision-based systems [5] and dedicated wireless positioning systems, such as frequency modulated continuous-wave [34] or UWB. It has to be pointed out that general purpose wireless networks (e.g., IEEE 802.11 wireless local area networks) do not offer a sufficient level of precision [29].

In [6], we have presented a novel tracking systems based on the integration of an absolute positioning system (through a UWB wireless network) with a local positioning system (constituted by the on-board odometer of a tricycle-like AGV). In particular, in order to take advantage of the intrinsic characteristics of UWB systems and to reduce the synchronization limitations, we adopt a Time Differences Of Arrivals (TDOA) approach to estimate the position of the AGV. Along with the classical TDOA approach, we also propose an innovative "Twin-receiver" TDOA (TTDOA) approach, in which two independent receivers are employed on the same AGV. While only a few examples of utilization of two distinct receivers for direct estimation of the AGV heading can be found [3,4], this approach has the advantage of reducing the estimation errors of the heading. Moreover, the absolute system positioning can offer some information about the heading when the odometer is not working properly or when the AGV is not moving (such as at the start-up of the AGV). In order to offer more insights on the performance of the tracking system, we will assume that the AGV follows a pre-determined path, thus ignoring any path-planning issue [31]. The movements of the AGV are also assumed to be decoupled from the estimates provided by the UWB-based tracking algorithm: in other words, there is no feedback between tracking and guidance systems [17]. While we focus on a single tracked AGV, the approach presented here could be generalized to encompass a generic number of AGVs, each following a target trajectory that can be computed as in [24].

The system presented in [6] is applicable to a wide spectrum of wireless technologies, since a generic distance estimation error is considered. In the present work, we focus on a UWB-based absolute positioning system, by considering (i) devices compliant with the IEEE 802.15.4a standard and (ii) a realistic model of the propagation channel. The market of IEEE 802.15.4a compliant transceivers is not growing fast, but a limited number of companies, for example Decawave, are already producing these devices [8]. Furthermore, in some applications, where more than a single AGV is involved, it is possible to further increase the system's accuracy by adopting some relative localization techniques [27].

This manuscript foresees two main parts, the former is devoted to the description of the proposed approach, while the latter contains the results of the experiments carried out to validate the model. In particular, the description of the framework is conduced in the following three sections. In Section 2, we give a mathematical characterization of the mobility model of the AGV. In Section 3, the UWB-based positioning system is accurately described. The EKF equations, characterizing the TDOA and TTDOA approaches, are presented in

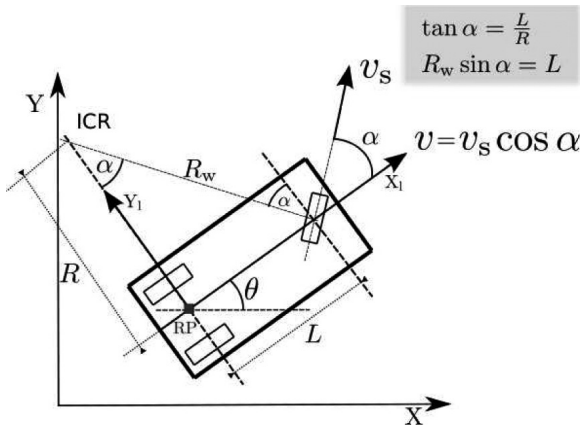

Fig. 1. The pose of the considered AGV.

Section 4. For what concerns the experimental validation, the Matlab-based simulator used to assess the performance of the proposed algorithms is described in Section 5, and their performance is investigated in Section 6. Finally, conclusions are drawn in Section 7.

2. The AGV and its mobility model

The considered AGV, pictured in Fig. 1, is a tricycle-like robot, with a two-wheel rear axis and a single wheel in the front axis, with both driving and steering functionalities.

We make a distinction between the robot local frame, with X_l and Y_l axes, and the absolute frame, with X and Y axes. The heading of the vehicle θ coincides with the angle between the two reference systems, while α denotes the steering direction of the front wheel with respect to the X_l axis. We assume that the EKF estimates the position of the AGV taking the point of coordinates (x, y) as the Reference Point (RP). Since the distance between the front and the rear axes is given by L (dimension: [m]), the curvature radius of the Instantaneous Center of Rotation (ICR) around which the vehicle rotates is given by $R_w = L/\sin(\alpha)$. Similarly, the vehicle rotates around the origin of the robot local frame with a radius of curvature $R = L/\tan(\alpha)$ and with an angular speed denoted as $w(t)$ (dimension: [rad/s]). Therefore, the vehicle moves along its direction with a speed $v(t) = Rw(t)$.

Under the assumptions of ideal wheels' rotation and of the lack of lateral slippage of the front wheel, the continuous-time dynamic model of the vehicle, with respect to the robot local frame, is given by the following system of equations [10]:

$$\begin{cases} v_{X_l}(t) = v_s(t)\cos[\alpha(t)] \\ v_{Y_l}(t) = 0 \\ w(t) \ = \frac{v_s(t)}{L}\sin[\alpha(t)] \end{cases}$$

where: $v_s(t)$ is the linear velocity of the steering wheel (dimension: [m/s]); v_{X_l} and v_{Y_l} represent the speeds along the X_l and Y_l axes, respectively – note that, because of the aforementioned assumption, $v_{Y_l}(t) = 0$ and $v_{X_l}(t) = v(t)$. The set of equations of the dynamic model in the absolute frame, can be obtained by means of a rotation of the angle θ:

$$\begin{cases} v_x(t) = v_s(t)\cos[\theta(t)]\cos[\alpha(t)] \\ v_y(t) = v_s(t)\sin[\theta(t)]\cos[\alpha(t)] \\ w(t) \ = \frac{v_s(t)}{L}\sin[\alpha(t)] \end{cases} \tag{1}$$

where $w(t)$ remains unchanged since it is rotation-invariant.

The state of the vehicle at the discrete time k is defined by the following vector:

$$\mathbf{s}_k \triangleq [x_k \, y_k \, \theta_k]^T \tag{2}$$

and its discrete-time update equation can be easily obtained from Eq. (1):

$$\begin{cases} x_{k+1} = x_k + T^o v_{sk}\cos(\theta_k)\cos(\alpha_k) \\ y_{k+1} = y_k + T^o v_{sk}\sin(\theta_k)\cos(\alpha_k) \\ \theta_{k+1} = \theta_k + \frac{T^o v_{sk}}{L}\sin(\alpha_k) \end{cases} \tag{3}$$

where: T^o (dimension: [s]) is the generic sampling time assumed to be known; v_{sk}, θ_k, and α_k are the discrete-time versions of the corresponding continuous-time quantities previously introduced.

According to Eq. (3), an AGV able to estimate v_{sk} and α_k every T^o, can also predict its dynamic state $\mathbf{s}_{k+1}$, under the assumption of knowing $\mathbf{s}_k$. For this reason, the AGV is equipped by an on-board odometer providing, with an average sample time equal to T^o, the following information: (i) the linear displacement of the front wheel at the sampling time, denoted as S (dimension: [m]) and equal to $T^o v_s(t)$; (ii) the steering angle, denoted by α (dimension: [rad]).[1]

3. UWB-based absolute positioning system

3.1. System architecture

The only use of the odometer for AGV tracking does not guarantee a sufficient accuracy, since its noisy mea-

[1] Even if practical odometers are typically affected by jitter, we ignore this issue in our work.

sures tend to lead to a cumulative error that increases over time. For this reason, we use a UWB-based absolute positioning system that provides periodic and reliable measurements of the AGV position. The nodes of the UWB positioning system, denoted as Anchor Nodes (ANs), have known positions. Additionally, ANs are assumed to be compliant with the IEEE 802.15.4a standard and to be synchronized by means of wired synchronization mechanisms (not addressed in this work). The estimation of the AGV position is achieved by measuring the time of arrivals of suitable ranging IEEE 802.15.4a packets sent by the ANs to the receiver(s) installed on the AGV.

At the physical level, an IEEE 802.15.4a packet is constituted by three distinct fields: a Synchronization HeadeR (SHR), a Packet HeadeR (PHR), and a Data Field (DF). In turn, the SHR is composed by two parts, a SYNChronization preamble (SYNC) and a Start of Frame Delimiter (SFD). The basic ranging mechanism between a pair of synchronized IEEE 802.15.4a devices (say A and B) is simple: (i) the node A sends a ranging packet after having inserted a timestamp on its DF; (ii) the node B receives the frame, extracts the original timestamp, and estimates the reception instant of the packet by identifying the SFD; (iii) from the timestamp and the reception instant, the node B can finally compute the Time of Flight (ToF) experienced by the frame and the inter-node distance, simply dividing the ToF by the speed of light ($c \simeq 3 \times 10^8$ m/s).

As anticipated in Section 1, the AGV can have two different UWB receiver configurations: (a) a classical TDOA configuration, with a single receiver; (b) the novel TTDOA configuration, with two independent receivers, each with its own antenna and its own independent clock generator. In the latter case, the receivers on board of the AGV are denoted, respectively, as Target Node A ($\mathrm{TN_A}$) and Target Node B ($\mathrm{TN_B}$), and they are assumed to be *not synchronized* with each other and with the ANs.

The ANs transmit periodically ranging packets that allow the TNs to estimate the distance between them. Every "collision domain" contains a maximum of 5 ANs (i.e., the AGV is connected to at most 5 ANs) and the EKF measurements' update is performed as soon as all 5 ANs have sent their own ranging packets. More precisely, we will consider a measurements' update period of duration equal to T^{u} (dimension: [s]). The estimates are affected by unavoidable errors and by a bias, due to the lack of synchronization with the ANs. The latter can be eliminated by simply computing the relative distances between the TNs and the ANs. The relative distances are obtained by subtracting the distance between the TNs and a Reference Node (RN), selected among the ANs, from the distance between the TNs and the AN. The ANs simultaneously transmitting to the AGV (i.e., in the same collision domain) are forced to transmit in orthogonal time slots in order to avoid Multi-User Interference (MUI).

In order to simplify the mathematical analysis, we assume that all the range estimates used by the EKF are obtained through Line-of-Sight (LOS) channels, without obstacles in any propagation path between the AN and the TNs. This strong assumption implies that the AGV can identify Non-Line-of-Sight (NLOS) propagation conditions [15], by exploiting the knowledge of its position and of the industrial environment where it is moving.

In order to evaluate the performance of a realistic UWB system, numerical simulations with Matlab will be carried out by considering: (i) a UWB signal compliant with the IEEE 802.15.4a standard, abiding by the power emission limit defined by the FCC [1]; (ii) a frequency-selective channel model defined by the IEEE 802.15.4a standardization group; (iii) the Energy Detector (ED) threshold-based TOA estimator originally introduced in [7].

3.2. The IEEE 802.15.4a channel model

Within the IEEE 802.15.4a working group, on the basis of measurement campaigns in several environments (outdoor and in three types of indoor scenarios – namely, residential, office, and industrial), a family of channel models for the high-frequency range ($3 \div 10$ GHz) has been derived [25]. In all considered cases, but for the industrial environment, the discrete-time channel impulse response (CIR) has been characterized with a customized Saleh-Valenzuela (SV) [30] model. According to the SV model, the CIR is composed by the following weighed sum of multipath components grouped in clusters:

$$h(t) = \sqrt{\mathrm{G}} \sum_{\ell=0}^{L_{\mathrm{c}}} \sum_{k=0}^{K} \alpha_{k,\ell} \exp(j\phi_{k,\ell}) \delta(t - T_\ell - \tau_{k,\ell}) \tag{4}$$

where: L_{c} is a Poisson random variable that defines the number of clusters of multipath; K is the maximum number of rays within a cluster; $\alpha_{k,\ell}$ is the weight of the k-th component of the ℓ-th cluster; T_ℓ is the delay of the ℓ-th cluster; $\tau_{k,\ell}$ is the delay of the k-th component with respect to the delay of the l-th cluster; G is the channel

gain parameter and it will be explained in the following; the phase shifts $\{\phi_{k,\ell}\}$ are independent and uniformly distributed in $[0, 2\pi]$. Without loss of generality, it can be assumed that

$$\sum_{\ell=0}^{L}\sum_{k=0}^{K}\alpha_{k,\ell}^2 = 1.$$

It is important to point out that in Eq. (4) the signal frequency distortion of the signal induced by the frequency selectivity of transmit and receive antennas has been ignored. However, it will be taken into account in the simulations carried out in Subsection 3.4 and Section 6. In particular, according to [9], the channel gain G is a function of the distance between source and receiver (d) and of the frequency (f), and can be expressed as follows [9]:

$$\begin{aligned}\mathrm{G}(f,d) &= \mathrm{G}(d)\mathrm{G}(f)\\ &= \mathrm{G}_0\left(\frac{d_0}{d}\right)^n\left(\frac{f_c}{f}\right)^{2+2k}.\end{aligned} \tag{5}$$

where: k is the frequency decay factor; n is the path-loss exponent; d_0 is a reference distance (dimension: [m]); f_c is the reference frequency (dimension: [Hz]); G_0 a reference parameter obtained by measuring the channel gain in d_0 and f_c, and it accounts for the noise figure and for the system losses. If, for sake of simplicity, one assumes that the transmitted pulse has a flat power spectrum in the frequency interval $[f_L, f_H]$, where f_L and f_H denote respectively, the lowest and the highest frequencies of the signal (dimension: [Hz]), then by integrating 5 in the interval $[f_L, f_H]$ it is possible to derive the following expression of the channel gain parameter G used in Eq. (4):

$$\begin{aligned}\mathrm{G} &= \int_{f_\mathrm{L}}^{f_\mathrm{H}}\mathrm{G}_0\left(\frac{d_0}{d}\right)^n\left(\frac{f_c}{f}\right)^{2+2k}\mathrm{d}f\\ &= \frac{\mathrm{G}_0(f_L^{-2k-1}-f_H^{-2k-1})}{(2k+1)f_c^{-2k-2}\left(\frac{d_0}{d}\right)^n}.\end{aligned} \tag{6}$$

At this point, the family of channel models can be obtained by varying the parameter that appear in the propagation model. In all simulations, we will consider the Channel Model 3 (CM3), defined in [25], suitable for an indoor office environment with strict LOS conditions.[2] The values of the main parameters of CM3 model are the same defined in [25].

3.3. The receiver and the TOA estimator

According to the IEEE 802.15.4a standard, both the SFD and SYNC are composed by a certain number of symbols. Furthermore, a symbol is in turn constituted by a series of modulated and shifted replica of a common signal pulse, denoted as $p(t)$, of duration T_p (dimension: [s]) and energy E_p (dimension: [J]). The signal $p(t)$ is the following root-raised cosine pulse [19]:

$$p(t)=\begin{cases}\frac{\sqrt{E_p}}{\sqrt{T_\mathrm{p}}}\left(1-\beta+4\frac{\beta}{\pi}\right) & t=0\\ \sqrt{E_p}\frac{\beta}{\sqrt{2T_\mathrm{p}}}\left[\left(1+\frac{2}{\pi}\right)\sin\left(\frac{\pi}{4\beta}\right)\right. & \\ \left.+\left(1-\frac{2}{\pi}\right)\cos\left(\frac{\pi}{4\beta}\right)\right] & t=\pm\frac{T_p}{4\beta}\\ \sqrt{E_p}\frac{4\beta}{\pi\sqrt{T_p}} & \\ \frac{\cos[(1+\beta)\pi t/T_p]+\frac{\sin[(1-\beta)\pi t/T_p]}{4\beta(t/T_p)}}{1-(4\beta t/T_p)^2} & \text{otherwise}\end{cases} \tag{7}$$

where $\beta \in [0, 1]$ is the roll-off factor.[3]

For the sake of simplicity, the following assumptions are made: (i) the receiver is always able to get coarsely synchronized with the ranging packet, by exploiting the SYNC symbols, with a precision of T_a (dimension: [s]); (ii) the SFD is constituted by a single symbol; (iii) unlike the standard IEEE 802.15.4.a, where a symbol is constituted by shifted and modulated replicas of $p(t)$, we assume that a symbol coincides with $p(t)$. The transmitted signal is centered at the frequency f_c, with a band-pass bandwidth $B \simeq 1/T_p$ and highest and lowest frequencies given by, respectively, $f_\mathrm{L} = f_c - B/2$ and $f_\mathrm{H} = f_c + B/2$.

The received signal, denoted as $r(t)$, can be written as:

$$r(t) = s(t) + n(t) \tag{8}$$

where $n(t)$ is an Additive White Gaussian Noise (AWGN) process with zero mean and two-sided power spectral density $N_0/2$, while $s(t)$ is given by the convolution between the pulse $p(t)$ and the CIR.

According to the expression of the CIR given in (4), $s(t)$ can be expressed as follows:

$$s(t)=\sqrt{\mathrm{G}}\sum_{\ell=0}^{L}\sum_{k=0}^{K}\alpha_{k,\ell}\exp(j\phi_{k,\ell})p(t-T_l-\tau_{k,\ell}). \tag{9}$$

On the basis of Eqs (8) and (9), the Signal-to-Noise Ratio (SNR) can be defined as GE_p/N_0.

[2] We observe that we have not chosen the industrial channel model (CM7) (that should apparently be a better choice), since it has been derived for metal-rich environment, with characteristics very different from which of the warehouses of interest in our project.

[3] Please note that Eq. (7) is different from that defined in the IEEE 802.15.4a standard [19], since, as recognized by several members of the IEEE P802.15 Working Group [2], $p(t)$ was incorrectly defined in [19].

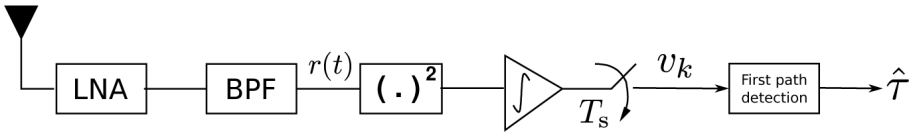

Fig. 2. Threshold-based TOA estimator based on an ED scheme.

The goal of the TOA estimator is to find the TOA of the Direct Path (DP), denoted as τ, on the basis of the received signal $r(t)$. Among the numerous existing estimators, with varying degrees of complexity and accuracy, we have considered a simple estimator, originally presented in [7], which is based on an Energy Detection (ED) receiver and on a threshold-crossing algorithm.

The ED receiver, shown in Fig. 2, is composed by a Band-Pass Filter (BPF), followed by a square-law device and an integrator, with an integration interval given by T_s (dimension: [s]).

The k-th output symbol of the integrator is expressed as v_k. Thanks to the strict LOS conditions, the DP is always present and its arrival time is uniformly distributed in $[0, T_\mathrm{a})$. The TOA estimator algorithm observes the output sequence $\{v_k\}$ for an observation interval T_obs (dimension: [s]), where $T_\mathrm{obs} > T_\mathrm{a}$. In other words, it observes N samples of the sequence, where $N_\mathrm{s} = \lfloor T_\mathrm{obs}/T_s \rfloor$. The sample v_k can be expressed as follows:

$$v_k = \int_{(k-1+n_\mathrm{TOA})T_s}^{(k+n_\mathrm{TOA})T_s} |r(t)|^2 \mathrm{d}t$$

$$k \in \{-n_\mathrm{TOA}+1, -n_\mathrm{TOA}+2, \ldots, N_\mathrm{m}\}$$

where $n_\mathrm{TOA} \triangleq \lfloor \tau/T_s \rfloor$ and $N_\mathrm{m} \triangleq N_\mathrm{s} - n_\mathrm{TOA}$.

Thanks to the LOS assumption, the sequence $\{v_k\}$ is always constituted by three distinct regions: (i) a leading noise-only region, (ii) a signal plus noise region, and a (iii) trailing noise-only region. The considered TOA estimator algorithm tries to determine the border between the first two regions. In particular, starting from the $(-n_\mathrm{TOA}+1)$-th sample, is compares each received value with a threshold η. The minimum value of k which satisfies the condition $v_k > \eta$ is the estimated TOA. In order to better investigate the impact of η, it is expedient to define the so-called Threshold-to-Noise Ratio (TNR), defined as η/N_0.

The choice of the optimized threshold η is critical. Since the estimator has to counteract thermal noise and fading, it is highly dependent on the SNR. However, in [7] the authors have shown that it is possible to define an SNR-independent threshold, that guarantees a performance quite close to the optimal one. In particular, once the target early-detection probability P_ed (e.g., the probability of electing a noise sample as the TOA) and N_0 are set, the corresponding TNR values can be determined by solving the following equations:

$$P_\mathrm{ed} = \mathbb{E}\left\{P_\mathrm{ed} | n_\mathrm{TOA}\right\} = 1 + \frac{(1-q_\mathrm{noise})^{N_\mathrm{TOA}} - 1}{N_\mathrm{TOA}\, q_\mathrm{noise}}$$

$$q_\mathrm{noise} = \exp\left(-\mathrm{TNR}\right) \sum_{i=0}^{M/2-1} \frac{\mathrm{TNR}^i}{i!}$$

where $M = 2WT_s$ and W represents the internal sample rate of the simulator (dimension: [Hz]), equal to $10/T_s$ in our simulation setup. In [7], the interested reader can find more details on the procedure used to set the threshold η.

3.4. Characterization of the estimation error

The ED estimator described in Subsection 3.3 allows to estimate the distance, denoted as r (dimension: [m]), between two UWB nodes. In order to derive the TDOA and TTDOA estimation algorithms, it is necessary to characterize the distance estimation error. Following the approach of [7], we define the BIAS as $\hat{r} - r$, where $\hat{r}$ is the output of the ED estimator. The standard deviation of the BIAS can be expressed as

$$\sigma_\mathrm{r} = \sqrt{\mathbb{E}\left\{(\hat{r}-r)^2\right\}}.$$

Note that, according to [7], $\sigma_\mathrm{r} \geqslant (cT_s)/\sqrt{12}$.

In order to characterize the BIAS of the estimator, one can measure its Probability Mass Function (PMF) and its standard deviation by means of MATLAB-based simulations, by considering the CM3 channel model and the ED-estimator defined in Subsection 3.3, with the parameters summarized in Table 1. In Fig. 3 (a), σ_r (solid lines) is shown as a function of the distance, considering two values of T_s: 1 ns and 2 ns, respectively. From the results in Fig. 3 (a), it emerges that the system with a halved integration window ($T_\mathrm{s} = 1$ ns) and a shorter pulse ($T_\mathrm{p} = 1$ ns) has a clear advantage (by a factor equal to 2) with respect to the estimator using a longer pulse ($T_\mathrm{p} = 2$ ns). The advantage reduces for longer distances. It is interesting to observe that the configuration with $T_\mathrm{s} = 1$ ns guarantees a standard de-

Table 1
Parameters of the UWB-based ED estimator used in the simulation

T_a	T_ob	T_s	T_p	β	P_ed	TNR	F	f_c
50 ns	60 ns	$\{1, 2\}$ ns	$\{1, 2\}$ ns	0.6	1e-3	14.8 dB	10 dB	4.49 GHz

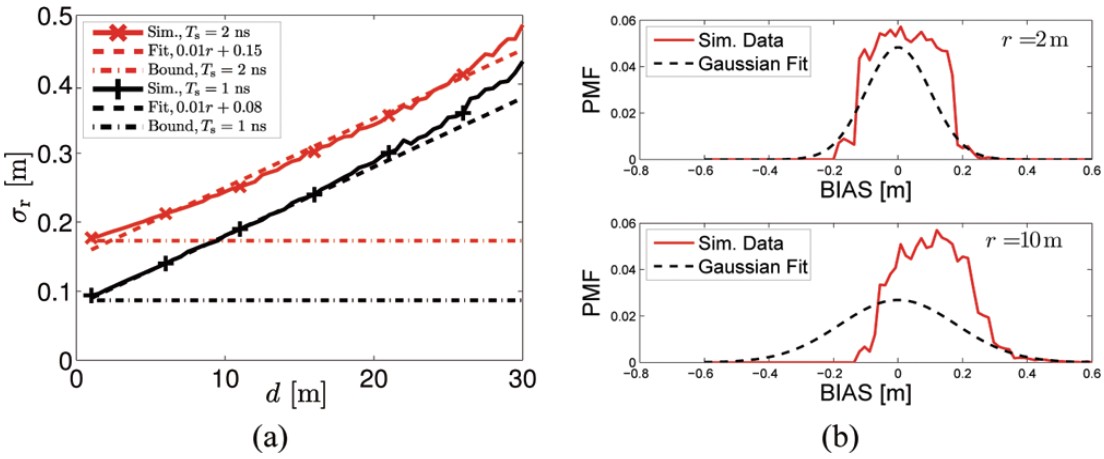

Fig. 3. (a) Standard deviation (σ_r) of the bias as a function of r (for two values of T_s) and (b) PMF of the BIAS for two values of r. In (a) the corresponding lower bounds (pointed lines) and linear fitting (dotted lines) are also shown. In (b) a Gaussian distribution with zero mean and standard deviation σ_r (dashed lines) is also shown.

viation smaller than 20 cm for all distances shorter than 10 m: therefore, it is an appealing choice for our localization system. Furthermore, from Fig. 3 (a) it emerges clearly that there is a linear relationship between σ_r and the distance, at least for values of $r < 20$ m. In particular, the standard deviation can be accurately approximated as follows:

$$\sigma_\mathrm{r} \simeq \sigma_{\mathrm{r}_0} r + \sigma_\mathrm{b}$$

where σ_{r_0} and σ_b are the slope and the intercept of the linear fitting, respectively. These results are in agreement with those presented in [21].

In Fig. 3 (b), the PMF of the BIAS is shown, setting $T_\mathrm{s} = T_\mathrm{p} = 1$ ns and considering two value of r (2 and 10 m, respectively). Two important observations can be carried out: (i) the PMF is asymmetric; (ii) the PMF tends to assume uniform distribution. For comparison, in Fig. 3 (b) the corresponding approximating Gaussian distributions (with the same mean and variance of the real PMFs) are shown. It can thus be concluded that the true PMFs are more "favorable," as the BIAS is more limited.

4. Extended Kalman filter-based tracking

EKF is a filtering technique suitable for estimating the state of discrete-time controlled processes governed by a non linear stochastic equation and affected by Gaussian noise. In particular, the *prediction step* allows to predict the future system state is predicted on the basis of the current state, while the *measurement* (or *update*) step allows to refine the prediction by means of indirect measurements of the system state.

In the remainder of this work, we will adopt the following notation: (i) the system state is denoted as $\mathbf{s} \in \mathbb{R}^n$, $n \in \mathbb{N}$; (ii) the measurement vector is denoted as $\mathbf{z} \in \mathbb{R}^m$, $m \in \mathbb{N}$; (iii) the symbol $\overline{\bullet}$ is used to denote an *a priori* prediction of quantity $\bullet$; (iv) the symbol $\hat{\bullet}$ is used to denote an *a posteriori* estimate of the quantity $\bullet$.

4.1. Prediction step

Under the assumption of a linear dependence on the process noise $w \in \mathbb{R}^n$, the prediction step of the EKF can be expressed as [16]

$$\begin{aligned}\overline{\mathbf{s}}_k &= f(\hat{\mathbf{s}}_{k-1}, \mathbf{u}_k) + \mathbf{w}_{k-1} \\ &= \begin{bmatrix} \overline{x}_k \\ \overline{y}_k \\ \overline{\theta}_k \end{bmatrix} = \begin{bmatrix} \hat{x}_{k-1} + \tilde{S}_k \cos(\hat{\theta}_{k-1}) \cos(\tilde{\alpha}_k) \\ \hat{y}_{k-1} + \tilde{S}_k \sin(\hat{\theta}_{k-1}) \cos(\tilde{\alpha}_k) \\ \hat{\theta}_{k-1} + \frac{\tilde{S}_k}{L} \sin(\tilde{\alpha}_k) \end{bmatrix} \\ &\quad + \mathbf{w}_{k-1} \end{aligned} \tag{10}$$

where $f(\cdot, \cdot)$ is a non-linear function that can be derived from 3, and

$$\mathbf{u}_k = [S_k \, \alpha_k]^T$$

is the control input vector containing data provided by the on-board odometer.

Given that the noise covariance matrix is $\mathbf{Q}$, the a priori error covariance matrix can be derived as follows:

$$\begin{aligned}\overline{\mathbf{P}}_k &= \mathbb{E}[(\mathbf{s}_k - \hat{\mathbf{s}}_k)(\mathbf{s}_k - \hat{\mathbf{s}}_k)^T] \\ &= \mathbf{A}\hat{\mathbf{P}}_{k-1}\mathbf{A}^T + \mathbf{Q} \end{aligned} \tag{11}$$

where: $\hat{\mathbf{P}}_{k-1}$ is the *a posteriori* error covariance matrix obtained from the previous step; $\mathbf{Q}$ is the noise covariance matrix, derived in Appendix A; $\mathbf{A}$, also derived in Appendix A, can be expressed as follows:

$$\mathbf{A} = \begin{bmatrix} 1 & 0 & -S_k \sin(\hat{\theta}_{k-1}) \cos(\alpha_k) \\ 0 & 1 & S_k \cos(\hat{\theta}_{k-1}) \cos(\alpha_k) \\ 0 & 0 & 1 \end{bmatrix}.$$

4.2. Measurement step

Under the assumption that the measurements' vector $\mathbf{z}$ is a non-linear function $h(\cdot)$ of the current system state, the relation between the measurement vector and the state vector can be expressed as follows:

$$\mathbf{z}_k = h(\mathbf{s}_k) + \mathbf{v}_k \tag{12}$$

where $\mathbf{v} \in \mathbb{R}^m$ denotes the noise associated to the measure, characterized by a covariance matrix $\mathbf{R}$. On the basis of Eq. (12), it is possible to define the matrix $\mathbf{H}$ as the Jacobian of $h(\cdot)$, with respect to the state vector $\mathbf{s}$, evaluated in $(\overline{\mathbf{s}}_\mathbf{k}, \mathbf{0})$:

$$H \triangleq \nabla \mathbf{h}_{|\mathbf{s}} \Big|_{(\overline{\mathbf{s}}_\mathbf{k}, \mathbf{0})}. \tag{13}$$

According to the consolidated EKF theory [16], the measurement update equations can be expressed as:

$$\begin{cases} \hat{\mathbf{s}}_k = \overline{\mathbf{s}}_k + \mathbf{K}_k \mathbf{e}_k \\ \hat{\mathbf{P}}_k = (\mathbf{I}_n - \mathbf{K}_k \mathbf{H}) \overline{\mathbf{P}}_k \end{cases} \tag{14}$$

where the Kalman gain $\mathbf{K}_k$ and the measurement error $\mathbf{e}_k$ are defined as

$$\mathbf{e}_k \triangleq \tilde{\mathbf{z}} - \mathbf{H}\overline{s}_k \tag{15}$$

$$\mathbf{K}_k \triangleq \frac{\overline{\mathbf{P}}_{k-1}\mathbf{H}^T}{\mathbf{H}\overline{\mathbf{P}}_{k-1}\mathbf{H}^T + \mathbf{R}}. \tag{16}$$

We recall that on the basis of the scenario described in Section 3, the measurement step is performed every T^{u}. Moreover, when the number of LOS ANs, denoted as N, is smaller than 4, the measurement step is not performed and the system relies simply on the prediction step – recall that the bi-dimensional TDOA problem requires 4 pseudo-range measures to estimate the position without any ambiguity.

4.2.1. TDOA method

Under the assumptions of (i) knowing the distance between the TN and the RN and (ii) having an estimate of the AGV dynamic state, the non-linear TDOA problem can be tackled by linearization, thus allowing the use of the simpler KF, instead of the EKF. An approach of this type, directly inspired by the approach presented in [26], is considered in this work.

We assume that the receiver $\mathrm{TN_A}$ is placed at the RP and, thus, is identified by the coordinates $(x_\mathrm{A}, y_\mathrm{A}) = (x, y)$, while the coordinates of the i-th AN are denoted as (x_i, y_i), $i \in \{1, 2, \ldots N\}$. Without loss of generality, we assume that the first AN is the RN. The linear measurement equation is the following:

$$\mathbf{z} = \mathbf{H}^{\mathrm{TDOA}}\mathbf{s}$$

where $\mathbf{H}^{\mathrm{TDOA}}$ is defined as in [26] by simply adding a third column in order to account for the presence of θ:

$$\mathbf{H}^{\mathrm{TDOA}} = \begin{bmatrix} x_2 - x_1 & y_2 - y_1 & 0 \\ x_3 - x_1 & y_3 - y_1 & 0 \\ \ldots & \ldots & \ldots \\ x_N - x_1 & y_N - y_1 & 0 \end{bmatrix}.$$

The measurement update equations are formally identical to Eq. (14):

$$\begin{cases} \hat{\mathbf{s}}_k = \overline{\mathbf{s}}_k + \mathbf{K}_k \mathbf{e}_k \\ \hat{\mathbf{P}}_k = \left(\mathbf{I}_{N-1} - \mathbf{K}_k \mathbf{H}^{\mathrm{TDOA}}\right) \overline{\mathbf{P}}_k \end{cases} \tag{17}$$

where $\mathbf{e}_k$ and $\mathbf{K}_k$ can be expressed, as shown in Appendix B.1, as:

$$\mathbf{e}_k = \mathbf{z} - \mathbf{H}^{\mathrm{TDOA}^T}\overline{s}_k = \mathbf{z} - \mathbf{u} - \hat{r_1}\mathbf{p}$$

$$\mathbf{K}_k = \frac{\overline{\mathbf{P}}_{k-1}\mathbf{H}^{\mathrm{TDOA}^T}}{\mathbf{H}^{\mathrm{TDOA}}\overline{\mathbf{P}}_{k-1}\mathbf{H}^{\mathrm{TDOA}^T} + \mathbf{R}^{\mathrm{TDOA}}}.$$

4.2.2. TTDOA method

As one can observe from Eq. (17), the TDOA method does not provide information about the heading θ of the vehicle. We now introduce the TTDOA technique, which, by employing two distinct UWB receivers, allows to reliably estimate the heading of the vehicle. The first receiver ($\mathrm{TN_A}$) is located on the longitudinal axis of the AGV at coordinates $(a, 0)$. The second receiver ($\mathrm{TN_B}$) is located on the traversal axis at the coordinates $(0, b)$ of the local frame. Note that we have set $a = L$ and $b = L/2$. In Fig. 4, we have indicated the positions of the receivers in the absolute frame, denoted, respectively, as $(x_\mathrm{A}, y_\mathrm{A})$ and $(x_\mathrm{B}, y_\mathrm{B})$, when the AGV is rotated by an angle θ. Therefore, the measurement equation provides an *indirect* estimation of θ and of the position of the RP, through direct estimation of

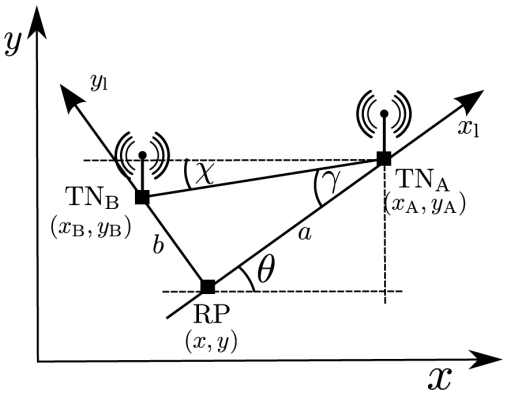

Fig. 4. Position of the $\mathrm{TN_A}$ and $\mathrm{TN_B}$ with respect to the reference point.

the positions of the two TNs. In fact, a rotation of $\hat{\theta}$ is used to obtain the position of the RP given the positions of the TNs. In particular, the non-linear measurement equation is the following:

$$\begin{aligned}\mathbf{z} &= h(\mathbf{s}) + \mathbf{v} \\ &= \begin{bmatrix} \tilde{x}_{\mathrm{A}_k} \\ \tilde{y}_{\mathrm{A}_k} \\ \tilde{x}_{\mathrm{B}_k} \\ \tilde{y}_{\mathrm{B}_k} \end{bmatrix} = \begin{bmatrix} x_k + a\cos(\theta_k) \\ y_k + a\sin(\theta_k) \\ x_k - b\sin(\theta_k) \\ y_k + b\cos(\theta_k) \end{bmatrix} + \mathbf{v}_k. \end{aligned} \tag{18}$$

The UWB receivers estimate independently their positions, without collaborating together and using the iterative Least Squares (LS) minimization technique presented in [18]. From Eq. (18), one obtains the Jacobian of $h(\cdot)$, with respect to the state $\mathbf{s}$, evaluated in $(\overline{\mathbf{s}}_\mathbf{k}, \mathbf{0})$:

$$\mathbf{H}^{\mathrm{TTDOA}} \triangleq \bigtriangledown_s \mathbf{h}|_{(\overline{\mathbf{s}}_\mathbf{k}, \mathbf{0})} = \begin{bmatrix} 1 & 0 & -a\sin(\overline{\theta}_k) \\ 0 & 1 & a\cos(\overline{\theta}_k) \\ 1 & 0 & -b\cos(\overline{\theta}_k) \\ 0 & 1 & -b\sin(\overline{\theta}_k) \end{bmatrix}.$$

The measurement update equations are formally identical to Eqs (14) and (17), i.e.,

$$\begin{cases} \hat{\mathbf{s}}_k = \overline{\mathbf{s}}_k + \mathbf{K}_k \mathbf{e}_k \\ \hat{\mathbf{P}}_k = (\mathbf{I}_4 - \mathbf{K}_k \mathbf{H}^{\mathrm{TTDOA}})\overline{\mathbf{P}}_k. \end{cases}$$

where $\mathbf{e}_k$ and $\mathbf{K}_k$ can be expressed, as shown in Appendix B.2, as:

$$\mathbf{e}_k = \mathbf{z} - \mathbf{H}^{\mathrm{TTDOA}^T} \overline{s}_k$$

$$\mathbf{K}_k = \frac{\overline{\mathbf{P}}_{k-1} \mathbf{H}^{\mathrm{TTDOA}^T}}{\overline{\mathbf{P}}_{k-1} \mathbf{H}^{\mathrm{TTDOA}^T} + \mathbf{R}^{\mathrm{TTDOA}}}.$$

5. Simulation setup

5.1. Description of the scenario

The tracking algorithms presented in the previous sections have been evaluated using a custom Matlab-based simulator. The first illustrative scenario (denoted as Scenario I), considered in most of the remainder of the paper (but in Subsection 6.4), is shown in Fig. 5.

The AGV (indicated by a rectangle) follows a predetermined path (solid gray line) in a warehouse-like environment. In particular, every T^o the AGV chooses its direction according to a simple path-following algorithm and generates a uniformly distributed speed in the interval $[v_s^{\min}, v_s^{\max}]$. For ease of comprehension, the instants at which the AGV reaches (on average) the first, second, and third turns are explicitly indicated in Fig. 5. The considered bi-dimensional environment also has some obstacles (thick black lines), that absorb the UWB signal, thus leading to NLOS propagation conditions. The ANs (indicated by a cross and a circle) are pseudo-randomly placed, abiding by the physical constraints imposed by the environment but without any optimization: a more regular ANs' placement will be considered in Subsection 6.4. Before evaluating the performance of the TDOA and TTDOA tracking algorithms, every receiver selects independently the nearest $N = 4$ ANs.

If not otherwise specified, the values of the relevant simulation parameters are those shown in Table 2. According to these values, $T^\mathrm{o} \ll T^\mathrm{u}$, and this implies that the measurement step is executed with a significant lower frequency than the prediction step.

It is worth mentioning that the standard deviations σ_S and σ_α characterize the error generated by the odometer at every step, i.e., every T^o.

The distance estimate used in the measurement step of the EKF is defined by the real-time execution of the ED-based estimator, configured with the parameters of Table 1, and by considering $T_\mathrm{p} = T_\mathrm{s} = 1$ ns. Therefore, in 26 the following values obtained in the training phase described in Subsection 3.4, have been used: $\sigma_{\mathrm{r}_0} =$ 0.01 m and $\sigma_\mathrm{b} = 0.08$ m.

5.2. Performance metrics

The performance of the proposed tracking algorithms, in terms of Root Mean Square Error (RMSE), is evaluated through Monte Carlo simulations of the scenario described in Subsection 5.1. In particular, the

Table 2
Parameters used in the simulation

σ_{S}	σ_{α}	σ_{r_0}	T^{o}	T^{u}	L	$v_s^{\max}$	$v_s^{\min}$
0.01 m	0.00175 rad	0.01 m	3.9 ms	125 ms	0.8 m	2.5 m/s	0.6 m/s

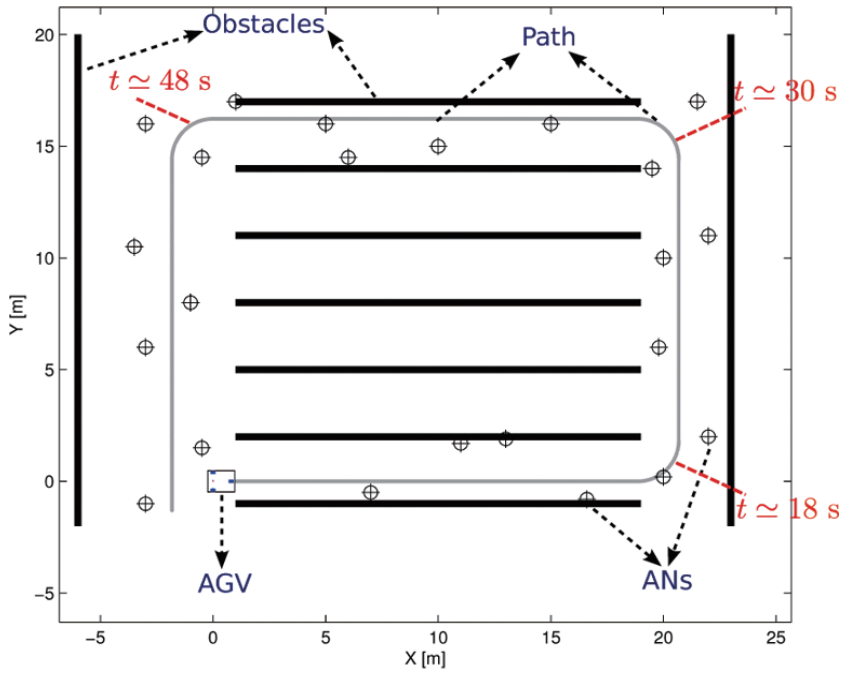

Fig. 5. A graphical representation of the Scenario I.

RMSE of the estimated AGV distance, with respect to its real position, is defined as follows:

$$\mathrm{RMSE}_{\mathrm{r}} \triangleq \sqrt{\mathbb{E}\{(\hat{x}-x)^2\}+\mathbb{E}\{(\hat{y}-y)^2\}} \quad (19)$$

while the RMSE of the AGV heading is

$$\mathrm{RMSE}_{\theta} \triangleq \sqrt{\mathbb{E}\{(\hat{\theta}-\theta)^2\}}. \quad (20)$$

Moreover, in order to assess the impact of the scenario geometry on the performance we consider the Geometric Dilution Of Precision (GDOP) and the Position Error Bound (PEB) [21]. Roughly speaking, the GDOP is an indicator of the impact of the geometry of the ANs on the position estimation errors, without considering the distance between ANs and TN. In the case of a TDOA system, it can be computed as in [22]:

$$\mathrm{GDOP}_{\mathrm{A}}^{\mathrm{TDOA}} = \frac{1}{\sigma_{\mathrm{r}_0}}\sqrt{\mathbf{G}_{\mathrm{A}}(1,1)+\mathbf{G}_{\mathrm{A}}(2,2))} \quad (21)$$

where $\mathbf{G}_{\mathrm{A}}$ indicates the matrix, introduced in Eq. (29), relative to the TN_{A} receiver. It can be shown that the minimum GDOP, equal to $2/\sqrt{N}$, is obtained when the ANs build a regular polygon around the TN.

The GDOP is a valid tool when $\sigma_{\mathrm{r}} = \sigma_{\mathrm{r}_0}$, but it is useless when σ_{r} depends on the distance, as in Eq. (26), since in the latter case the geometry of the network is less important. In this context, the PEB is more relevant, since it is defined as the lower bound of $\mathrm{RMSE}_{\mathrm{r}}$, thus allowing to assess the impact of both the distance of the ANs and the network geometry [21]. The expression of the PEB for a TOA system, denoted as $\mathrm{PEB}^{\mathrm{TOA}}$, is the following [21]:

$$\mathrm{PEB}_{\mathrm{A}}^{\mathrm{TOA}} = \sqrt{\frac{\sum_{k=1}^{n} A_k}{\sum_{k=1}^{n} A_k c_k \sum_{k=1}^{n} A_k s_k - \left(\sum_{k=1}^{n} A_k c_k s_k\right)^2}}$$

where $c_k = \cos(\theta_k^{\mathrm{A}})$, $s_k = \sin(\theta_k^{\mathrm{A}})$, and

$$A_k = \frac{1}{\sigma_{\mathrm{r}_0}^2 ||\mathrm{TN}_{\mathrm{A}} - \mathrm{AN}_k||^2} + \frac{2}{||\mathrm{TN}_{\mathrm{A}} - \mathrm{AN}_k||^2}. \quad (22)$$

The angle between the x-axis of the absolute frame and the segment between the origin and TN_{A} is denoted as θ_k^{A}, while $||\mathrm{TN}_{\mathrm{A}} - \mathrm{AN}_k||$ is the length of the segment itself (the distance). We have considered the PEB for a TOA system since (i) it is easier to obtain than the

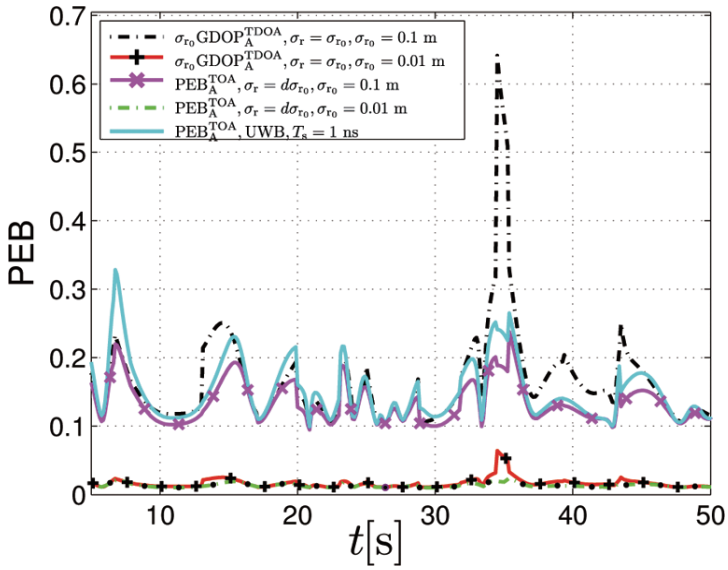

Fig. 6. GDOP and PEB experienced by the AGV along the considered path, by considering two constant values of σ_{r_0}, respectively, 0.1 m and 0.01 m. The PEB curve corresponding to the real UWB positioning system is also shown.

PEB of a TDOA system and (ii) both PEBs are very similar, as shown in the simulation analysis carried out in Subsection 5.1. We finally observe that, in the case of constant σ_r (e.g., when it is independent from the distance), Eq. (22) reduces to $A_k = \sigma_{r_0}^{-2}$ and, then, the PEB becomes identical to the GDOP multiplied by σ_{r_0}, i.e.,

$$\mathrm{PEB}^{\mathrm{TOA}} = \sigma_{r_0}\mathrm{GDOP}^{\mathrm{TOA}}. \tag{23}$$

Equation (23) is important since it allows to compare the $\mathrm{PEB}^{\mathrm{TOA}}$, which is relative to a TOA system, with the scaled $\mathrm{GDOP}^{\mathrm{TDOA}}$ carried out by a TDOA system, in order to validate this approximation. This comparison is carried out in Fig. 6 for an AGV following the path in Fig. 5 and for two values of σ_{r_0} (0.1 m and 0.01 m, respectively). For both values of σ_{r_0}, the PEB curves compare favorably with the scaled $\mathrm{GDOP}^{\mathrm{TDOA}}$ curves of a TDOA system. Therefore, it is possible to consider $\mathrm{PEB}^{\mathrm{TOA}}$ as a good indicator of the real $\mathrm{PEB}^{\mathrm{TDOA}}$. Furthermore, in both cases there are no significant peaks of the PEB, thus showing that the ANs are well positioned. Finally, in Fig. 6 we also show the $\mathrm{PEB}^{\mathrm{TOA}}$ obtained by using the real UWB positioning system in the same scenario. It emerges that the UWB system exhibits a PEB comparable to that of the case with $\sigma_{r_0} = 0.1$ m.

6. Performance evaluation

In this section, we analyze the performance of the proposed AGV tracking systems, by means of numerical simulations, from various viewpoints. In particular, this section has the following goals, targeted in corresponding subsections: (i) to compare the performance of the TDOA and TTDOA algorithms, in order to verify the presence of an effective performance gain of the solution with two receivers (Subsection 6.1); (ii) to assess the validity of the noise Gaussian approximation, which is expedient to use of the EKF technique (Subsection 6.2); (iii) to accurately evaluate the performance of the TTDOA algorithm as a function of several system parameters (Subsection 6.3); (iv) to assess the impact, on the system performance, of the ANs' placement and of the presence of moving obstacles (Subsection 6.4).

6.1. *Performance comparison of TDOA and TTDOA algorithms*

The first task (i.e., the comparison between the TDOA and TTDOA algorithms) has been performed without using the ED-based estimator. Instead, in the simulator distance estimates are generated as in Eq. (25), where the Gaussian noise has zero mean and standard deviation independent of the distance ($\sigma_r = \sigma_{r_0}, \forall r$). In the upper and lower subfigures of Fig. 7, RMSE_r and RMSE_θ are shown, respectively, as functions of time.[4] In both cases, two values of

[4] In this section, if not differently specified, the shown RMSEs are evaluated *after* the update step of the EKF (i.e., every T^u s): this leads to smoother and more readable figures.

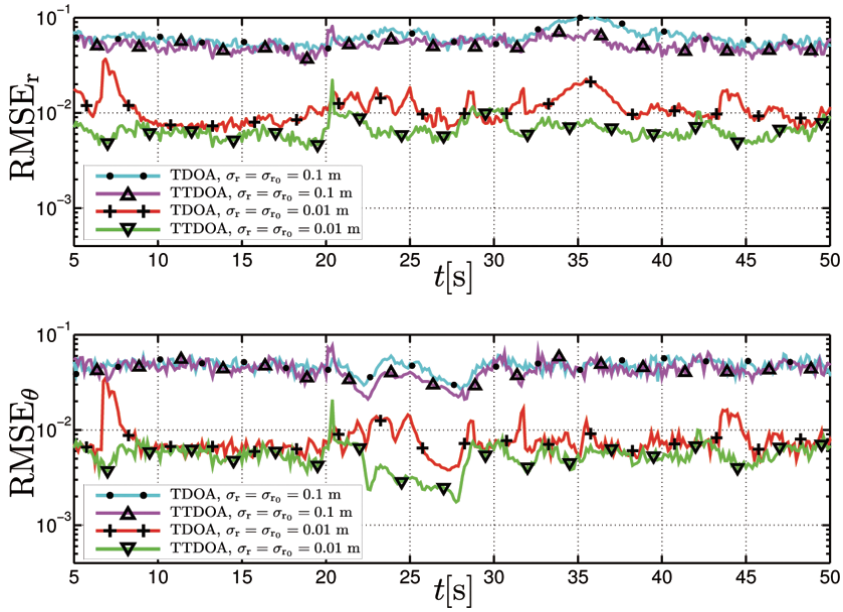

Fig. 7. $\mathrm{RMSE_r}$ (upper subfigure) and RMSE_θ (lower subfigure), as functions of time, with the TDOA and the TTDOA algorithms, respectively. Two values of σ_{r_0} (0.1 m and 0.01 m) are considered.

$\sigma_{\mathrm{r}_i} = \sigma_{\mathrm{r}_0}$ are considered: namely, 0.1 m and 0.01 m. Figure 7 shows that when $\sigma_{\mathrm{r}_0} = 0.1$ m, the performance of both TDOA and TTDOA approaches is limited. In this situation, the UWB positioning system provides too noisy measures and, therefore, does not contribute to reduce the localization errors, but is only effective in preventing error accumulation. For this reason, the performances of the TDOA and TTDOA algorithms are identical.

The comparison with $\sigma_{\mathrm{r}_0} = 0.01$ m is more meaningful, since in this case the UWB positioning system allows to significantly reduce the localization errors. In this case, the TTDOA technique, by taking advantage of the twin receiver configuration, significantly reduces both $\mathrm{RMSE_r}$ and RMSE_θ, with respect to the TDOA approach. From the results in Fig. 7, it emerges that the TTDOA approach also reduces the estimation oscillations, thus leading to a smoother AGV movement.[5] Despite these improvements, the RMSEs still show a few peaks. They are due to the combination of several causes. Notably, the peak at $t = 25$ s is probably due to the corresponding peak of the PEB observed in Fig. 6. On the other hand, the remaining RMSE peaks appear in correspondence to the turns of the path and, therefore, are probably generated by the odometer. This is reasonable since, during turns, both sources of error of the odometer (i.e., α and S) have relevant impacts, while in the straight segments the error on α has a limited impact.

In the following subsections (but for Subsection 6.4), we will only consider the TTDOA algorithm, as this is more promising than the traditional TDOA algorithm, at least when the estimation errors are sufficiently small.

6.2. *Impact of the gaussian approximation of the noise distribution*

We now investigate the impact of the noise Gaussian approximation on the system performance. More precisely, we compare the results obtained by effectively using the ED-based estimator in the simulator with those obtained by generating the estimation bias according to a Gaussian distribution. It is important to observe that, in both cases, the EKF uses Eq. (26) in order to determine the value of σ_{r_i}, using the same values of the parameters σ_{r_0} and σ_{b}. Therefore, the EKF "sees" the same underlying distance estimator (Gaussian error with variance given by Eq. (26)), but in the simulator two radically different approaches are used.

The obtained results are shown in Fig. 8, along with the results obtained with σ_{r} independent of the distance, for two values of σ_{r_0} (0.1 m and 0.01 m, respectively).

[5] In the perspective of coupling the localization algorithm with the driving algorithm of the AGV, it is particularly important to minimize the estimation oscillations, in order to avoid abrupt changes of direction.

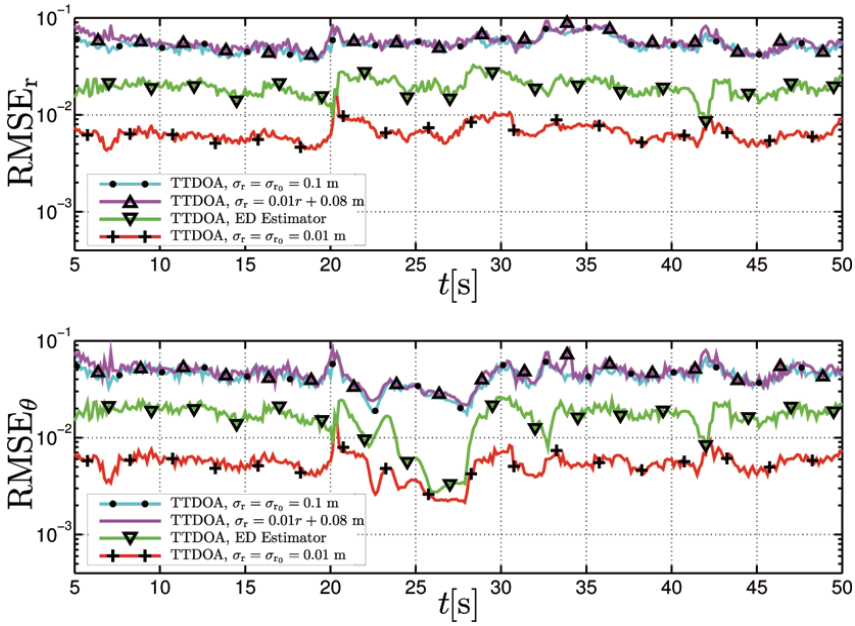

Fig. 8. $\mathrm{RMSE_r}$ as a function of time (and thus position), obtained with the TTDOA algorithm. Two values of $\sigma_{\mathrm{r_0}}$ are considered (0.1 and 0.01 m), Gaussian error, ED-based estimator.

Coherently with the conclusions reached with the PEB analysis (Fig. 6), the system $\sigma_{\mathrm{r}} = \sigma_{\mathrm{r_0}} = 0.01$ m outperforms the others, thanks to its much lower PEB, and it thus acts as a benchmark. Conversely, the ED-based system exhibits a performance significantly better than that of the other systems and it sometimes reaches the same performance level of the benchmark, despite the fact of having a quite smaller PEB. This discrepancy can be motivated by observing the shape of the PMF of the bias in Fig. 3. In fact, is easy to understand that the represented PMF leads (on average) to smaller errors than a Gaussian-like distribution, thanks to its smaller tails (especially for negative values of the bias). Furthermore, these results allow to validate the Gaussian approximation (expedient for the EKF design). In fact, the real error distribution leads to better performance than that with an artificially generated Gaussian distribution.

According to the findings of this subsection, in the following we focus only on the use of the ED-based estimator coupled with the TTDOA algorithm, ignoring the other system configurations.

6.3. Impact of system parameters

Once the channel model and the TTDOA estimator have been fixed, there are four remaining design parameters ("degrees of freedom"): (i) T^{u}; (ii) T^{o} (iii); σ_{S}; (iv) σ_α. For easy of comprehension, in our analysis we have not changed T^{o}, implicitly assuming that the adopted value is the one guaranteeing the optimal tradeoff between accuracy and update frequency.

We initially focus on the parameters related to the odometer (namely, σ_{S} and σ_α), by considering an increased value of the standard deviation σ_{S} (0.001 m) and a reduced value of the standard deviation σ_α (0.00175 rad). In particular, we have considered 4 different configurations obtained by combining the values $\sigma_{\mathrm{S}} = 0.01$ m, 0.001 m and $\sigma_\alpha = 0.0175$ rad, 0.00175 rad, while the remaining parameters are configured as in Tables 1 and 2. The choice of considering the value $\sigma_{\mathrm{S}} = 0.001$ m can be justified by observing that the previously used value ($\sigma_{\mathrm{S}} = 0.01$ m) was quite pessimistic, since it leads to an error around $10 \div 20$ cm per meter covered by the AGV.

The obtained performance is shown in Fig. 9, in terms of RMSE_r and RMSE_θ as functions of time. According to the results of Fig. 9, it emerges that σ_α has a limited (almost negligible) impact on the performance. This is probably due to the predominance of straight segments in the considered path of Fig. 5, with respect to the small number of turns. On the opposite hand, the standard deviation σ_{s} significantly influences the performances. In fact, the value $\sigma_{\mathrm{s}} = 0.001$ m leads to a significant performance improvement and to a reduction of the oscillations.

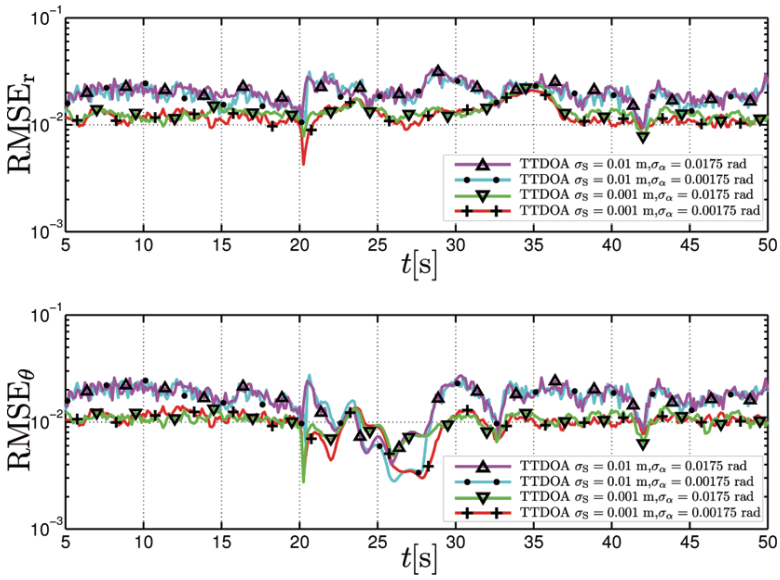

Fig. 9. $\mathrm{RMSE_r}$ (upper subfigure) and RMSE_θ (lower subfigure), as functions of time, in the CM3 UWB channel, using the ED estimator and with the TTDOA algorithm. Two values of σ_s (0.01 m and 0.001 m), and two values of σ_α (0.0175 rad and 0.00175 rad) are considered.

It is now interesting to investigate the possibility of further improving the performance by reducing the time interval T^u between two consecutive EKF measurement steps to 32.5 ms, thus increasing the update frequency of the UWB positioning system. According to the IEEE 802.15.4a standard, this is a reasonable assumption, since the duration of a ranging packet usually does not exceed 5 ms.[6] Hence, since there are 5 ANs in every collision domain, T^u can be reduced, even considering a time guard between successive ranging packets, by at least a factor of 4, thus yielding to an update interval $T^\mathrm{u} = 32.5$ ms.

By combining the values $\sigma_\mathrm{S} = 0.01$ m, 0.001 m and $T^\mathrm{u} = 32.5$ ms, 125 ms, it is possible to obtain 4 different configurations (referred to as (a), (b), (c), and (d)), whose parameters are summarized in Table 3. The remaining parameters are configured as in Tables 1 and 2, including a single value for σ_α (0.00175 rad), since it has a negligible impact, as shown in Fig. 9. The configuration (a) acts as a negative benchmark since it has the "less favorable" set of parameters ($\sigma_\mathrm{S} = 0.01$ m and $T^\mathrm{u} = 125$ ms). On the opposite, the configuration (d), characterized by smaller values of σ_S and of T^u, is the one with the "most favorable" set of parameters. The remaining configurations (b) and (c) lead to a single improvement, in terms of either σ_S or T^u.

[6]More precisely, the value of 5 ms is a worst-case scenario, obtained by considering the longest SHR preamble (4160 symbols) and the lowest modulation data-rate (110 Kbit/s) [19].

Table 3
Improved configuration settings and corresponding performance results (relative to Fig. 10) in various scenarios

	(a)	(b)	(c)	(d)
T^u [ms]	125	125	32.5	32.5
σ_S [m]	0.01	0.001	0.01	0.001
$\overline{\mathrm{RMSE}_r}$ [m]	0.0428	0.0129	0.0265	0.00877
$\max\{\mathrm{RMSE}_r\}$ [m]	0.0795	0.0225	0.0450	0.0126
$\overline{\mathrm{RMSE}_\theta}$ [°]	0.2928	0.1265	0.1945	0.0814
$\max\{\mathrm{RMSE}_\theta\}$ [°]	2.4000	0.5613	1.4086	0.4274

In Fig. 10, the performances of the new configurations, in terms of RMSE_r and RMSE_θ as functions of time, are directly compared. In order to shed light on the impact of T^u, in Fig. 10 a shorter time window (between 15 s and 20 s) is considered and, more importantly, the shown RMSEs are sampled *after* the prediction step of the EKF (i.e., every T^o). In order to quantitatively characterize the qualitative evaluation offered by the graphical analysis, in Table 3 we clearly list the time-averaged values and the maximum values of $\mathrm{RMSE_r}$ and RMSE_θ.

By observing Fig. 10 and Table 3, it emerges that increasing the update frequency and reducing σ_S lead to similar beneficial effects: (i) to significantly reduce the absolute values of the RMSEs; (ii) to achieve weaker local oscillations. The joint adoption of these improvements lead to very small RMSEs' values, almost constant over the time, as in the case of the configuration (d).

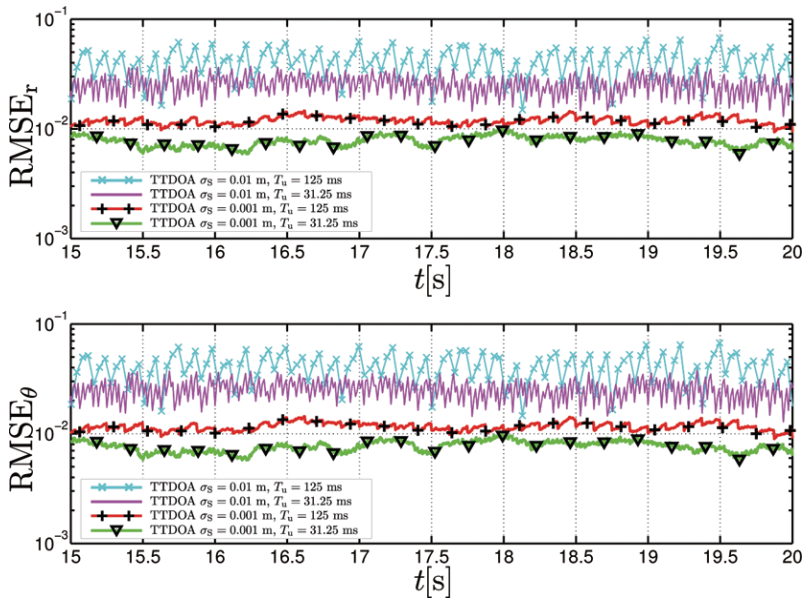

Fig. 10. $\mathrm{RMSE_r}$ (upper figure) and RMSE_θ (lower figure), as functions of time, obtained with the TTDOA algorithm, setting $\sigma_{\mathrm{r}_0} = 0.01$ m. The dot-dashed line curve refers to the case with constant σ_{r}. The others three curves correspond to the configurations in Table 3. (Colours are visible in the online version of the article; http://dx.doi.org/10.3233/ICA-2012-0390)

It is interesting to note that configuration (d) exhibits a sub-centimeter average $\overline{\mathrm{RMSE}}_r$ (9 mm), with a maximum value of 1.3 cm, and a small value of average $\overline{\mathrm{RMSE}}_\theta$ (less then $0.1°$). These values seem to be satisfactory for the tracking of AGVs in industrial applications related to goods' displacement in factories. However, before integrating our approach into a real guidance system, there are some questions that are still unaddressed. For example, an algorithm for the placement of the ANs is still needed. Finally, it is not yet clear if the amplitude of the oscillations are compatible with the requirements of real-time guidance systems. This is the subject of our current research activity.

6.4. *Impact of anchors' placement and of moving obstacles*

Until now we have considered a scenario (which will be referred to as Scenario I) characterized by pseudo-randomly placed ANs and a quasi-symmetric path covered by the AGV. In this subsection, we consider a more regular scenario, denoted as Scenario II, with a symmetric path followed by the AGV and more regularly placed ANs: the new scenario is shown in Fig. 11. In particular, 12 ANs are located along the straight segments, while the remaining 16 ANs are located around the four corners of the path. The total number of ANs (namely, 28) is thus slightly increased with respect to that (equal to 24) of Scenario I and it corresponds to an ANs' density approximately equal to 0.05 $\mathrm{AN/m^2}$. For ease of comprehension, the instants at which the AGV reaches (on average) the first, second, and third turns are explicitly indicated in Fig. 11.

In Fig. 12, the performances in both scenarios (with the parameters of Table 2) are directly compared in terms of RMSE_r and RMSE_θ as functions of time. It should be noticed that because of the different lengths of the paths followed by the AGV, it is not possible to compare the corresponding performance curves in a pointwise manner. However, it is still possible to compare the performance in terms of average behavior. As expected, it can be observed that Scenario II does not offer advantages in terms of absolute values: however, in this scenario the RMSEs have a quite smoother behavior. Furthermore, by comparing Figs 12 and 7 it emerges that when using realistic ED-based receiver, the performance gap between TDOA and TTDOA schemes becomes significantly larger. This further motivates the choice of adopting the TTDOA scheme.

Finally, in order to further evaluate the robustness of our approaches, in Scenario II we have considered the presence of a couple of moving obstacles. More specifically, we assume to have two additional vehicles, one preceding the tracked AGV, and the second following it, moving at the same (random) speed of the AGV. Obviously, more sophisticated mobility models of the ob-

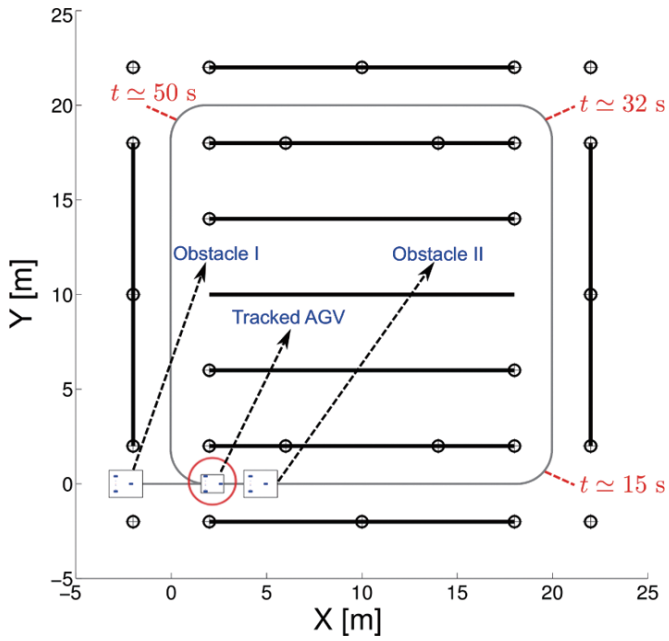

Fig. 11. Graphical representation of Scenario II. The starting positions of the moving obstacles are also shown.

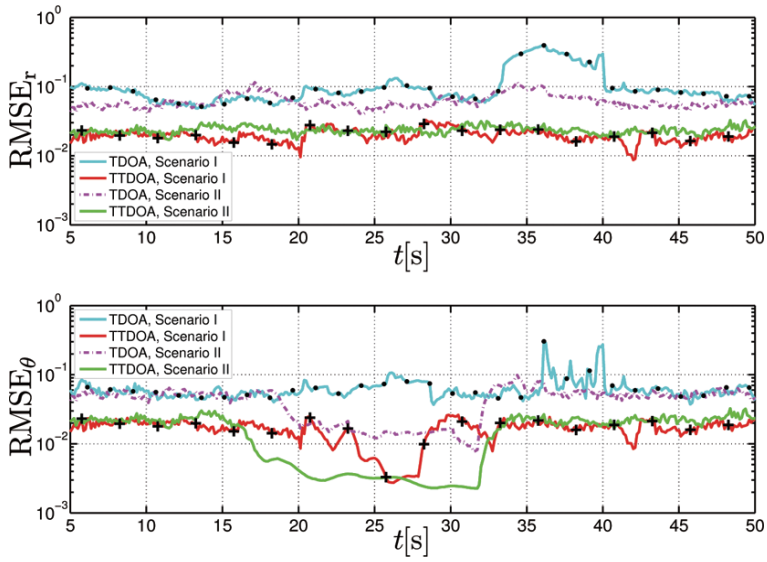

Fig. 12. $\mathrm{RMSE_r}$ (upper figure) and RMSE_θ (lower figure), as functions of time, obtained with the TDOA and the TTDOA algorithms, using the parameters of Table 2, and by considering Scenario I and Scenario II.

stacles, as those presented in [12], could be considered. The obstacles are slightly wider and longer than the tracked AGV. The starting positions of the AGV itself and of obstacles is shown in Fig. 11. More precisely, by considering the respective RPs: (i) the AGV starts in $(1.8, 0)$ m; (ii) the starting position of Obstacle I is $(-2.9, 0)$ m; (iii) the starting position of Obstacle II is $(4.15, 0)$ m.

In Fig. 13, the performances obtained in Scenario II, with and without the moving obstacles, are directly compared in terms of RMSE_r and RMSE_θ as functions of time. According to the results of Fig. 13, it emerges that this specific configuration of moving obstacles has a limited impact on the performance and it determines a

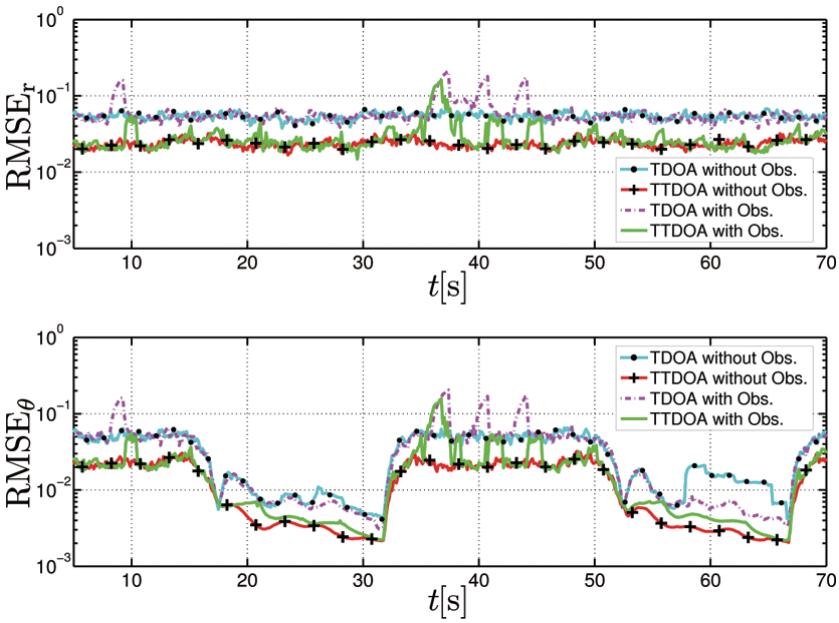

Fig. 13. $\mathrm{RMSE_r}$ (upper figure) and RMSE_θ (lower figure), as functions of time, obtained with the TDOA and the TTDOA algorithms, using the parameters of Table 2 and Scenario II. Two configurations are considered: (i) the first without obstacles; (ii) the second with obstacles.

penalty loss only in a short fraction of the path followed of the AGV. More precisely, the loss refers to the path segments where the TDOA/TTDOA algorithm cannot be executed because of the too small number of visible ANs. In these cases, the RMSEs exhibit relevant peaks (almost one order of magnitude higher than the typical values) whose heights and durations are more pronounced when using the TDOA algorithm. Conversely, as one expects, the TTDOA approach is more robust against the presence of moving obstacles.

7. Conclusions

In this work, we have presented two tracking algorithms for an AGV moving in an industrial scenario, based on an EKF that combines measures from an on-board odometer (local positioning system) and from a UWB-based wireless localization system (absolute positioning system). The main contributions of this work can be summarized as follows.

- We have proved that the standard deviation of UWB-based ranging measurements linearly scales with the distance. We have also shown that a Gaussian approximation is not accurate for modeling the error distribution of UWB-based ranging measurements, since it tends to significantly overestimate the predicted distance error.
- We have presented a novel, to the best of our knowledge, solution (namely, the TTDOA algorithm) that fuses together the location information provided by an on-board odometer with that provided by an absolute UWB-based positioning system.
- The proposed scheme exhibits a centimeter-grade accuracy in bi-dimensional environments with an AN spatial density approximately equal to $0.05\ \mathrm{AN/m^2}$. This performance level has been obtained in strongly faded environment, without a refined optimization of the placement of the ANs, and by considering standard equipment (odometer and UWB transceivers).
- The TTDOA algorithm outperforms the classical single receiver-based approach (TDOA) in all the tested operative conditions. The performance gap between the two approaches in normal conditions (e.g., without obstacles) is proportional to the precision of the UWB system. Moreover, according to the experimental results, the advantages offered by the TTDOA solution are more relevant in non-ideal scenarios, namely, with realistic UWB receivers and with the presence of moving obstacles that temporarily obstruct the visibility of the ANs.

Future extensions of this work may include:

- the derivation of an analytical planning technique for optimized ANs' placement;

- coupling of the proposed positioning system with the AGV guidance system;
- effective real-time execution of the proposed algorithms.

Moreover, we are currently planning to implement the proposed solutions in a real testbed in order to perform accurate measurement campaigns.

Acknowledgment

The work of S. Busanelli was partially supported by the Spinner consortium. The authors would like to thank F. De Mola, M. Magnani, and M. Casarini (all of Elettric80 Spa) for providing relevant information and for their continuous support and help.

A. Analytical derivation of the prediction step

In this section, the matrices $\mathbf{A}$ and $\mathbf{Q}$ used in the a priori error covariance matrix update Eq. (11), will be derived. In particular, the matrix $\mathbf{A}$, defined as the Jacobian of $f(\cdot,\cdot)$ with respect to the state vector $\mathbf{s}$ and evaluated in $(\hat{\mathbf{s}}_{\mathbf{k-1}}, \mathbf{u_k}, \mathbf{0})$, can be obtained as follows:

$$\mathbf{A} \triangleq \bigtriangledown \mathbf{s} f|_{(\hat{\mathbf{s}}_{\mathbf{k-1}}, \mathbf{u_k}, \mathbf{0})} = \begin{bmatrix} 1 & 0 & -S_k \sin(\hat{\theta}_{k-1})\cos(\alpha_k) \\ 0 & 1 & S_k \cos(\hat{\theta}_{k-1})\cos(\alpha_k) \\ 0 & 0 & 1 \end{bmatrix}.$$

In order to derive the noise covariance matrix $\mathbf{Q}$ it is necessary to analyze the errors affecting the odometer measurements. In particular, we can define the vector $\tilde{\mathbf{u}}_k$ as follows:

$$\tilde{\mathbf{u}}_k = \begin{bmatrix} \tilde{S}_k \\ \tilde{\alpha}_k \end{bmatrix} = \begin{bmatrix} S_k + w'_k(1) \\ \alpha_k + w'_k(2) \end{bmatrix} \tag{24}$$

where the vector $\mathbf{w}' = (w'_k(1), w'_k(2))$ is a bivariate Gaussian random vector with zero mean and with the following (known) covariance matrix:

$$\mathbf{Q}^{\mathrm{odo}} = \begin{bmatrix} \sigma_{\mathrm{S}}^2 & 0 \\ 0 & \sigma_\alpha^2 \end{bmatrix}.$$

Now, $\mathbf{Q}$ is related to the covariance matrix $\mathbf{Q}^{\mathrm{odo}}$ by the following relationship and it can be derived as follows:

$$\mathbf{Q} = \mathbf{B}\mathbf{Q}^{\mathrm{odo}}\mathbf{B}^T$$

where $\mathbf{B}$ is the Jacobian of $f(\cdot,\cdot)$ with respect to the control vector $\mathbf{u}$:

$$\mathbf{B} \triangleq \bigtriangledown \mathbf{u} f|_{(\hat{\mathbf{s}}_{\mathbf{k-1}}, \mathbf{u_k}, \mathbf{0})} = \begin{bmatrix} \cos(\hat{\theta}_{k-1})\cos(\alpha_k) & -S_k \sin(\hat{\theta}_{k-1})\sin(\alpha_k) \\ \sin(\hat{\theta}_{k-1})\cos(\alpha_k) & -S_k \cos(\hat{\theta}_{k-1})\sin(\alpha_k) \\ \dfrac{\sin(\alpha_k)}{L} & \dfrac{S_k \cos(\alpha_k)}{L} \end{bmatrix}.$$

B. Analytical derivation of the measurement step

B.1. TDOA

Let define with r_i the (real) distance between the TN and the i-th AN, i.e.,

$$r_i = \sqrt{(x_{\mathrm{A}} - x_i)^2 + (y_{\mathrm{A}} - y_i)^2} \qquad i = 1, \ldots, N.$$

Then, the measured relative distances can be expressed as

$$\tilde{r}_i = r_i + n_i + b_i \qquad i = 1, \ldots, N \tag{25}$$

where: $b_i = b$, $\forall i$ and b is the synchronization bias, with respect to the ANs; and the noise samples $\{n_i\}$ have a multi-variate Gaussian distribution with zero mean and the following diagonal covariance matrix:

$${\Sigma_{\mathrm{r}}}^2 = \mathrm{diag}(\sigma_{\mathrm{r}_1}^2, \sigma_{\mathrm{r}_2}^2, \ldots, \sigma_{\mathrm{r}_N}^2).$$

It is important to point out that the Gaussianity assumption is necessary to employ the EKF technique, but as shown in Subsection 3.4, the real distribution of the distance estimation error is not Gaussian. In Subsection 3.4 it has been proved the existence of a linear relationship between σ_{r} and the distance, according with, $\sigma_{\mathrm{r}_i}^2$ can be expressed as follows:

$$\sigma_{\mathrm{r}_i}^2 = (\sigma_{\mathrm{r}_0} r_i + \sigma_{\mathrm{b}})^2. \tag{26}$$

The relative distances between the i-th AN and the RN are given by:

$$d_{i,1} = r_i - r_1 \qquad i = 2, \ldots, N$$

while the noisy relative distances are given by:

$$\tilde{d}_{i,1} = \tilde{r}_i - \tilde{r}_1 + n_i - n_1 \qquad i = 2, \ldots, N. \tag{27}$$

Therefore, the relative distances from the 2-nd to the N-th anchor are affected by a Gaussian vector with zero mean and with the following $(N-1) \times (N-1)$ covariance matrix:

$$\mathbf{R}^{\mathrm{TDOA}} = \mathbf{Q}^{\mathrm{TDOA}}\, {\sigma_{\mathrm{r}}}^2\, \mathbf{Q}^{\mathrm{TDOA}^T} \tag{28}$$

$$= \begin{bmatrix} \sigma_{\mathrm{r}_1}^2 + \sigma_{\mathrm{r}_2}^2 & \sigma_{\mathrm{r}_1}^2 & \ldots & \sigma_{\mathrm{r}_1}^2 \\ \sigma_{\mathrm{r}_1}^2 & \sigma_{\mathrm{r}_1}^2 + \sigma_{\mathrm{r}_3}^2 & \ldots & \sigma_{\mathrm{r}_1}^2 \\ \ldots & \ldots & \ldots & \ldots \\ \sigma_{\mathrm{r}_1}^2 & \sigma_{\mathrm{r}_1}^2 & \ldots & \sigma_{\mathrm{r}_1}^2 + \sigma_{\mathrm{r}_N}^2 \end{bmatrix}.$$

where $\mathbf{Q}^{\mathrm{TDOA}}$ is a $(N-1)\times N$ matrix defined as:

$$\mathbf{Q}^{\mathrm{TDOA}} = \begin{bmatrix} -1 & 1 & 0 & \dots & 0 \\ -1 & 0 & 1 & \dots & 0 \\ \dots & \dots & \dots & \dots & \dots \\ -1 & 0 & 0 & \dots & 1 \end{bmatrix}.$$

From Eq. (15), it follows that $\mathbf{K}_k$ and $\mathbf{e}_k$ can be expressed as

$$\begin{aligned} \mathbf{e}_k &= \mathbf{z} - \mathbf{H}^{\mathrm{TDOA}^T}\overline{s}_k \\ &= \mathbf{z} - \mathbf{u} - \hat{r_1}\mathbf{p} \\ \mathbf{K}_k &= \frac{\overline{\mathbf{P}}_{k-1}\mathbf{H}^{\mathrm{TDOA}^T}}{\mathbf{H}^{\mathrm{TDOA}}\overline{\mathbf{P}}_{k-1}\mathbf{H}^{\mathrm{TDOA}^T} + \mathbf{R}^{\mathrm{TDOA}}} \end{aligned}$$

where $\hat{r_1}$ is the distance between the RN and the predicted AGV position $[\overline{s}_k(1)\,,\,\overline{s}_k(2)]^T$, and the vectors $\mathbf{p}$ and $\mathbf{u}$ are defined as follows [26]:

$$\mathbf{p} = \begin{bmatrix} \tilde{d}_{2,1} \\ \dots \\ \tilde{d}_{N,1} \end{bmatrix}$$

$$\mathbf{u} = \frac{1}{2}\begin{bmatrix} \left(x_2^2+y_2^2\right) - \left(x_1^2+y_1^2\right) - \tilde{d}_{2,1}^2 \\ \left(x_3^2+y_3^2\right) - \left(x_1^2+y_1^2\right) - \tilde{d}_{2,1}^2 \\ \dots \\ \left(x_N^2+y_N^2\right) - \left(x_1^2+y_1^2\right) - \tilde{d}_{N,1}^2. \end{bmatrix}.$$

B.2. TTDOA

The covariance matrix of the noise vector $\mathbf{v}_k$, denoted as $\mathbf{R}^{\mathrm{TTDOA}}$, can be obtained by deriving the covariance matrix of the TDOA estimations of the positions of $\mathrm{TN_A}$ and $\mathrm{TN_B}$, denoted, respectively, as $\mathbf{G}_{\mathrm{A}}$ and $\mathbf{G}_{\mathrm{B}}$. One thus obtains:

$$\mathbf{R}^{\mathrm{TTDOA}} = \begin{bmatrix} \mathbf{G}_{\mathrm{A}} & \mathbf{I}_2 \\ \mathbf{I}_2 & \mathbf{G}_{\mathrm{B}} \end{bmatrix}.$$

where $\mathbf{G}_{\mathrm{A}}$ and $\mathbf{G}_{\mathrm{B}}$ are functions of the covariance matrix $\mathbf{R}^{\mathrm{TDOA}}$ introduced in Eq. (28). The matrix $\mathbf{G}_{\mathrm{A}}$ (the same considerations hold for $\mathbf{G}_{\mathrm{B}}$) can be obtained as shown in [22] as follows:

$$\mathbf{G}_{\mathrm{A}} = \left(\mathbf{M}_{\mathrm{A}}^T\mathbf{R}^{\mathrm{TTDOA}}\mathbf{M}_{\mathrm{A}}\right)^{-1} \tag{29}$$

where $\mathbf{M}_{\mathrm{A}}$ it is the Jacobian of the Eq. (27) with respect to the coordinates of $\mathrm{TN_A}$ (i.e., $(x_{\mathrm{A}}, y_{\mathrm{A}})$:

$$\mathbf{M}_{\mathrm{A}} = \begin{bmatrix} \frac{x_{\mathrm{A}}-x_2}{r_2} - \frac{x_{\mathrm{A}}-x_1}{r_1} & \frac{y_{\mathrm{A}}-y_2}{r_2} - \frac{y_{\mathrm{A}}-y_1}{r_1} \\ \frac{x_{\mathrm{A}}-x_3}{r_3} - \frac{x_{\mathrm{A}}-x_1}{r_1} & \frac{y_{\mathrm{A}}-y_3}{r_3} - \frac{y_{\mathrm{A}}-y_1}{r_1} \\ \dots & \dots \\ \frac{x_{\mathrm{A}}-x_N}{r_N} - \frac{x_{\mathrm{A}}-x_1}{r_1} & \frac{y_{\mathrm{A}}-y_N}{r_N} - \frac{y_{\mathrm{A}}-y_1}{r_1} \end{bmatrix}.$$

We finally obtain the expressions of $\mathbf{e}_k$ and $\mathbf{K}_k$:

$$\begin{aligned} \mathbf{e}_k &= \mathbf{z} - \mathbf{H}^{\mathrm{TTDOA}^T}\overline{s}_k \\ \mathbf{K}_k &= \frac{\overline{\mathbf{P}}_{k-1}\mathbf{H}^{\mathrm{TTDOA}^T}}{\overline{\mathbf{P}}_{k-1}\mathbf{H}^{\mathrm{TTDOA}^T} + \mathbf{R}^{\mathrm{TTDOA}}}. \end{aligned}$$

References

[1] Title 47, Section 15 of the Code of Federal Regulations Sub-Part F: Ultra-wideband, FCC, Washington, DC, USA, October 2005.

[2] 802.15 WNG. Meeting minutes IEEE P802.15-07/0666r0, March 2007.

[3] R. Anderson and D.M. Bevly, Estimation of slip angles using a model based estimator and GPS, in *Proceedings of the American Control Conference*, volume 3, Boston, MA, USA, June 2004, pp. 2122–2127.

[4] D.M. Bevly, J. Ryu and J.C. Gerdes, Integrating INS sensors with GPS measurements for continuous estimation of vehicle sideslip, roll, and tire cornering stiffness, *IEEE Transactions on Intelligent Transportation Systems* **7**(4) (December 2006), 483–493.

[5] M.S. Bittermann, I.S. Sariyildiz and Ö. Ciftcioglu, Visual perception in design and robotics, *Integrated Computer-Aided Engineering* **14**(1) (2007), 73–91.

[6] S. Busanelli and G. Ferrari, UWB-based tracking of autonomous vehicles with multiple receivers, in A.C.-C. Chang, M. Li, C. Rong, C.Z. Patrikakis and D. Slezak, eds, *Communication and Networking, Part I*, volume 119 of *Communications in Computer and Information Science*, Springer, 2010, pp. 188–198.

[7] D. Dardari, C.C. Chong and M.Z. Win, Threshold-based time-of-arrival estimators in uwb dense multipath channels, *IEEE Trans Commun* **56**(8) (August 2008), 1366–1378.

[8] Decawave DW4aSS1000. http://www.decawave.com/scensor.html.

[9] M. Dohler, J. Liu, R.M. Buehrer, S. Venkatesh and B. Allen, Large- and medium-scale propagation modelling, in: *Ultra-wideband: Antennas and Propagation for Communications, Radar and Imaging*, B. Allen, M. Dohler, E.E. Okon, W.Q. Malik, A.K. Brown and D.J. Edwards, eds, chapter 14, Wiley, 2007, pp. 283–306.

[10] G. Dudek and M. Jenkin, *Computational principles of mobile robotics*. Cambridge University Press, Cambridge, UK, 2nd edition, July 2010.

[11] ECMA International. High rate ultra wideband PHY and MAC standard, December 2005.

[12] A. Fujimori, T. Fujimoto and G. Bohacs, Formatted navigation of mobile robots using a modified leader-follower technique, *Integrated Computer-Aided Engineering* **15**(1) (2008), 71–84.

[13] S. Gezici and H.V. Poor, Position estimation via ultra-wideband signals, *Proceedings of the IEEE* **97**(2) (February 2009), 386–403.

[14] S. Gezici, T. Zhi, G.B. Giannakis, H. Kobayashi, A.F. Molisch, H.V. Poor and Z. Sahinoglu, Localization via ultra-wideband radios: a look at positioning aspects for future sensor networks, *IEEE Signal Processing Mag* **22**(4) (July 2005), 70–84.

[15] I. Guvenc, C.C. Chong, F. Watanabe and H. Inamura, NLOS identification and weighted least-squares localization for UWB systems using multipath channel statistics, *EURASIP J Adv Signal Process* **2008**(36) (January 2008).

[16] S. Haykin, *Adaptive filter theory*, Prentice Hall, Upper Saddle River, NJ, USA, 2002.

[17] M. Hentschel, O. Wulf and B. Wagner, A hybrid feedback controller for car-like robots–combining reactive obstacle avoidance and global replanning, *Integrated Computer-Aided Engineering* **14**(1) (2007), 3–14.

[18] K.C. Ho and W.W. Xu, An accurate algebraic solution for moving source location using TDOA and FDOA measurements, *IEEE Trans. Signal Processing* **52**(9) (September 2004), 2453–2463.

[19] IEEE 802.15.4a. Part 15.4: Wireless Medium Access Control (MAC) and Physical Layer (PHY) Specifications for Low-Rate Wireless Personal Area Networks (WPANs). Amendment 1: Add Alternate PHYs, August 2007.

[20] A. Islam, U. Iqbal, J.M. Pierre Langlois and A. Noureldin, Implementation methodology of embedded land vehicle positioning using an integrated GPS and multi sensor system, *Integrated Computer-Aided Engineering* **17**(1) (2010), 69–83.

[21] D.B. Jourdan and N. Roy, Optimal sensor placement for agent localization, *ACM Trans. Sensor Networks* **4**(3) (May 2008), 1–40.

[22] N. Levanon, Lowest GDOP in 2-D scenarios, *IEE Proceedings-Radar, Sonar and Navigation* **147**(3) (June 2000), 149–155.

[23] G. MacGougan, K. O'Keefe and R. Klukas, Tightly-coupled GPS/UWB integration, *Journal of Navigation* **63**(1) (2010), 1–22.

[24] J.S. Mejía and D.M. Stipanović, Computational receding horizon approach to safe trajectory tracking, *Integrated Computer-Aided Engineering* **15**(2) (2008), 149–161.

[25] A.F. Molisch, D. Cassioli, C.-C. Chong, S. Emami, A. Fort, B. Kannan, J. Karedal, J. Kunisch, H.G. Schantz, K. Siwiak and M.Z. Win, A comprehensive standardized model for ultrawideband propagation channels, *IEEE Trans Antennas Propagat* **54**(11) (November 2006), 3151–3166.

[26] M. Nájar and J. Vidal, Kalman tracking based on TDOA for UMTS mobile location, in: *Proc. IEEE International Symposium on Personal and Indoor and and Mobile Radio Commun*, (vol. 1), San Diego, CA, USA, September 2001, pp. B–45–B–49.

[27] J.D. Ni, D. Arndt, P. Bgo, K. Dekome and J. Dusl, Ultra-wideband tracking system design for relative navigation. Technical Report SC-CN-23740., NASA, May 2010.

[28] G.G. Rigatos, Extended Kalman and particle filtering for sensor fusion in motion control of mobile robots, *Math Comput Simul* **81**(3) (November 2010), 590–607.

[29] C. Röhrig and F. Künemund, WLAN based pose estimation for mobile robots, in: *Proc. on Intl. Conf. Federation of Automatic Control* (IFAC), Seoul, Korea, July 2008, pp. 10433–10438.

[30] A. Saleh and R. Valenzuela, A statistical model for indoor multipath propagation, *IEEE J Select Areas Commun* **5**(2) (February 1987), 128–137.

[31] R. Solea and U. Nunes, Trajectory planning and sliding-mode control based trajectory-tracking for cybercars, *Integrated Computer-Aided Engineering* **14**(1) (2007), 33–47.

[32] L. Teslić, I.Škrjanc and G. Klančar, EKF-based localization of a wheeled mobile robot in structured environments, *Springer Journal of Intelligent and Robotic Systems* **62**(2) (May 2011), 187–203.

[33] Ubisense System Overview. http://ubisense.net.

[34] M. Vossiek, L. Wiebking, P. Gulden, J. Weighardt and C. Hoffmann, Wireless local positioning-concepts, solutions, applications, in: *Proceedings Radio and Wireless Conference* (RAWCON), Boston, MA, USA, 2003, pp. 219–224.

[35] M.Z. Win and R.A. Scholtz, Impulse radio: how it works, *IEEE Commun Letters* **2**(2) (February 1998), 36–38.